




# Fast and Balanced Charge Transport Enabled by Solution-Processed Metal Oxide Layers for Efficient and Stable Inverted Perovskite Solar Cells

Jing Zhang , James Mcgettrick, Kangyu Ji, Jinxin Bi, Thomas Webb, Xueping Liu , Dongtao Liu, Aobo Ren, Yuren Xiang, Bowei Li, Vlad Stolojan, Trystan Watson, Samuel D. Stranks, and Wei Zhang\* 

**Metal oxide charge transport materials are preferable for realizing long-term stable and potentially low-cost perovskite solar cells (PSCs). However, due to some technical difficulties (e.g., intricate fabrication protocols, high-temperature heating process, incompatible solvents, etc.), it is still challenging to achieve efficient and reliable all-metal-oxide-based devices. Here, we developed efficient inverted PSCs (IPSCs) based on solution-processed nickel oxide (NiO<sub>x</sub>) and tin oxide (SnO<sub>2</sub>) nanoparticles, working as hole and electron transport materials respectively, enabling a fast and balanced charge transfer for photogenerated charge carriers. Through further understanding and optimizing the perovskite/metal oxide interfaces, we have realized an outstanding power conversion efficiency (PCE) of 23.5% (the bandgap of the perovskite is 1.62 eV), which is the highest efficiency among IPSCs based on all-metal-oxide charge transport materials. Thanks to these stable metal oxides and improved interface properties, ambient stability (retaining 95% of initial PCE after 1 month), thermal stability (retaining 80% of initial PCE after 2 weeks) and light stability (retaining 90% of initial PCE after 1000 hours aging) of resultant devices are enhanced significantly. In addition, owing to the low-temperature fabrication procedures of the entire device, we have obtained a PCE of over 21% for flexible IPSCs with enhanced operational stability.**

## 1. Introduction

Inverted perovskite solar cells (IPSCs) have attracted worldwide attention owing to their low-temperature processing and remarkable compatibility with large-area and flexible devices.<sup>[1–3]</sup> Driven by numerous recent advancements including defect passivation, interface engineering, and the introduction of novel charge transport materials (CTMs), etc., the record power conversion efficiency (PCE) of IPSCs (24.3%) is on par with that of the n-i-p counterparts (25.7%) as of writing, and the lifetimes of IPSCs also have been enhanced considerably.<sup>[3–10]</sup> Reviewing the recent development of high-performance IPSCs, CTMs are of critical importance, because their fundamental properties including work function, conductivity, carrier mobility, etc. have direct impacts on the performance of the resultant devices.<sup>[11,12]</sup> For the typical p-type CTMs in IPSCs, poly(triaryl amine) (PTAA), poly(3-hexylthiophene-2,5-diyl) (P3HT), [2-(9H-carbazol-9-yl) ethyl] phosphonic acid (2-PACz) and nickel oxide (NiO<sub>x</sub>) are popular materials used in high-performance IPSCs,<sup>[4,6–9]</sup> whereas

phenyl-C<sub>61</sub>-butyric acid methyl ester (PCBM), C<sub>60</sub> and other organic materials including n-type hexaazatrinaphtho[2,3-c][1,2,5]thiadiazole (HATNT), perylene diimide (PDI)-based compounds have been widely used as the n-type CTMs.<sup>[6–8,13–16]</sup>

Among the aforementioned CTMs, metal oxides are promising candidates owing to their extraordinary features such as good band alignment, ease of fabrication, low cost, no toxicity, and superior inherent stability.<sup>[17–22]</sup> For p-type metal oxide materials, nickel oxide (NiO<sub>x</sub>) has gained enormous attention recently in the best-performing IPSCs as compared to other candidates such as Cu<sub>2</sub>O, VO<sub>x</sub>, MoO<sub>x</sub> etc.,<sup>[23–25]</sup> thanks to its versatile preparation methods, tunable work function, high optical transmittance in visible wavelength range, excellent stability and low cost.<sup>[26–28]</sup> More importantly, the fabrication protocols of NiO<sub>x</sub> are various, including but not limited to sol–gel, sputtering, and atomic layer deposition (ALD), etc.<sup>[29–31]</sup> By optimizing the interface between perovskite and NiO<sub>x</sub>, the PCEs of the state-of-the-art IPSCs based on NiO<sub>x</sub> have reached over 23%.<sup>[4,10,32]</sup> Comparatively, the choice of


Dr. J. Zhang, J. Bi, T. Webb, Dr. X. Liu, D. Liu, Dr. A. Ren, Dr. Y. Xiang, Dr. B. Li, Dr. V. Stolojan, Prof. W. Zhang  
Advanced Technology Institute (ATI), University of Surrey, Guildford, Surrey GU2 7XH, UK

E-mail: wz0003@surrey.ac.uk

Dr. J. Mcgettrick, Prof. T. Watson  
SPECIFIC, College of Engineering, Swansea University, Bay Campus SA1 8EN, Swansea UK

K. Ji, Prof. S. D. Stranks  
Cavendish Laboratory, University of Cambridge, JJ Thomson Avenue, Cambridge CB3 0HE, UK

Prof. S. D. Stranks  
Department of Chemical Engineering & Biotechnology, University of Cambridge, Philippa Fawcett Drive, Cambridge CB3 0AS, UK

 The ORCID identification number(s) for the author(s) of this article can be found under <https://doi.org/10.1002/eam2.12595>.

DOI: 10.1002/eam2.12595

n-type metal oxide materials is rather limited in inverted devices because of either involving high-temperature treatment ( $>150\text{ }^{\circ}\text{C}$ ) or incompatible solvents with the underlying perovskite layer.<sup>[33–36]</sup> One demonstrated example is ZnO, however, its hygroscopic nature makes it incompatible with long-term stable devices.<sup>[20,37,38]</sup> Additionally, previous studies have unveiled that unstable or non-uniform n-type material could accelerate the degradation process of the perovskite layer, because they either are hygroscopic or fail to effectively block  $\text{O}_2$  and/or  $\text{H}_2\text{O}$  from entering into the active layer.<sup>[37,39,40]</sup> In this context, more efforts have been hence dedicated to the exploration of suitable n-type metal oxide materials.  $\text{SnO}_2$ , a wonderful n-type metal oxide that has been broadly used in the best-performing PSCs with n-i-p structure, has rarely been explored in the IPSCs, due to the challenges including high post-annealing temperature ( $>150\text{ }^{\circ}\text{C}$ ) and solvent incompatibility (usually  $\text{H}_2\text{O}$ ) with perovskite. A few prior research works have attempted to use  $\text{SnO}_2$  in IPSCs fabricated by either atomic layer deposition (ALD) or spin-coating, but the device performances are not ideal as compared to those using PCBM or  $\text{C}_{60}$  as the CTM.<sup>[33,34,41–43]</sup> In addition to obtaining a compact and smooth CTM layer, the main challenge towards realizing high-performance devices is how to manage the interfaces between perovskite and metal oxides, and achieve fast and balanced charge extraction/transfer.

In this work, we demonstrate highly efficient IPSCs with solution-processed metal oxides as both n-type and p-type CTMs. In particular,  $\text{NiO}_x$  as the most successful p-type material in high-performance IPSCs, will be used as the hole transport material (HTM). As for the n-type CTM, we demonstrate that  $\text{SnO}_2$  nanoparticles (NPs) can be directly deposited on top of the perovskite layer at room temperature via a simple solution-based approach, without inducing the decomposition of the underlying structures. We further modified the interfaces of both  $\text{NiO}_x$ /perovskite and perovskite/ $\text{SnO}_2$  to reduce the defects and hence mitigate non-radiative recombinations at these interfaces, enabling fast and balanced charge transfer across the entire device. Moreover, after incorporating PCBM, the band mismatch between  $\text{SnO}_2$  and perovskite could be minimized, thus, the accumulation of charges at the perovskite/ETM interface can be alleviated. Another benefit of PCBM is that the oxygen vacancies within the  $\text{SnO}_2$  layer can be passivated, that is, compared with  $\text{SnO}_2$ -only devices, electron traps are fewer in the  $\text{SnO}_2$ /PCBM-based counterparts. Conductivity, which will be discussed later, is enhanced as well for the  $\text{SnO}_2$ /PCBM combination, providing smoother pathways for electrons compared with a single  $\text{SnO}_2$  or single PCBM counterparts. As a result, a remarkable short-circuit photocurrent density ( $J_{\text{sc}}$ ) of  $23.66\text{ mA cm}^{-2}$  was obtained (we note the  $J_{\text{sc}}$  limit is  $24.83\text{ mA cm}^{-2}$  for the perovskite with a bandgap of  $1.62\text{ eV}$ ) by utilizing  $\text{NiO}_x$  and  $\text{SnO}_2$  as the main CTMs.<sup>[44]</sup> Consequently, the champion device delivers an outstanding PCE of 23.5% ( $V_{\text{oc}} = 1.20\text{ V}$ ,  $J_{\text{sc}} = 23.66\text{ mA cm}^{-2}$ , fill factor = 82.96%, efficiency = 23.53%), which is the highest efficiency among PSCs based on all-metal-oxide CTMs. Additionally, with the assistance of these compact metal oxides as internal encapsulation layers, barriers against oxygen and water have been formed, contributing to the prolonged stability of the resultant IPSCs. Subsequently, these all-metal-oxide-based IPSCs reserve 95% of their original PCEs after 1-month storage (temperature =  $25\text{ }^{\circ}\text{C}$ , relative humidity = 45%, dark, unencapsulated). Besides, these all-metal-oxide-based IPSCs have demonstrated excellent thermal and photostability. Thanks to the low-temperature fabrication protocols of all the functional layers, we achieved flexible IPSCs with the same configuration, delivering an exceptional PCE of over 21% with enhanced stability.

## 2. Results and Discussion

We note that the p-type properties  $\text{NiO}_x$  are closely related to the nickel vacancies (or self-doping of  $\text{Ni}^{3+}$ ),<sup>[45]</sup> and the conductivity of pristine  $\text{NiO}_x$  is limited due to the large ionization energy of the Ni site.<sup>[46]</sup> In this context, we doped the pristine  $\text{NiO}_x$  with a small amount of copper ( $\text{Cu:NiO}_x$ ).<sup>[47]</sup> The concentration of Cu has been optimized, as a result, the ratio of Cu/Ni is 5% here. Because a high Cu ratio would sharply reduce the optical transmittance, while a low ratio can not guarantee sufficient conductivity, this conclusion agrees with many previous studies.<sup>[48–50]</sup> Compared with organic HTMs, the resultant  $\text{Cu:NiO}_x$  presents the best hole mobility (Table S1). To further minimize the interfacial charge recombination and accumulation, a thin layer of [2-(9H-carbazol-9-yl) ethyl] phosphonic acid (2-PACz) was used to passivate the interface of  $\text{Cu:NiO}_x$ /perovskite because the 2-PACz has exhibited excellent hole selectivity and reduced interfacial recombination.<sup>[51,52]</sup> We then carried out photoluminescence (PL) and time-resolved photoluminescence (TRPL) studies to probe the HTM/perovskite interface. As shown in Figure 1a, noticeable PL quenching can be observed after copper doping and 2-PACz passivation, indicating enhanced hole collection ability of the resultant HTM. And the TRPL result (Figure 1b) is in agreement with PL data, where copper doping in conjunction with 2-PACz passivation led to a reduced decay lifetime from 19.74 to 4.88 ns (Table S2). Afterwards, we studied the interface between the perovskite and solution-processed  $\text{SnO}_2$  layer. We note that the quenching effect of the single  $\text{SnO}_2$  is rather limited (Figure 1c) because the  $\text{SnO}_2$  prepared from the low-temperature process may contain numerous defects, and the work function may not align well with the photoactive layer.<sup>[53]</sup> We then tried to passivate the perovskite/ $\text{SnO}_2$  interface by depositing PCBM either on top (perovskite/ $\text{SnO}_2$ /PCBM) or beneath the  $\text{SnO}_2$  layer (perovskite/PCBM/ $\text{SnO}_2$ ). We find that the former is a better choice as the required post-annealing of  $\text{SnO}_2$  layer ( $100\text{ }^{\circ}\text{C}$ , 40 min) is likely to trigger the agglomeration of the pre-deposited PCBM.<sup>[54,55]</sup> The TRPL data are, indeed, in agreement with our speculation: the average decay time reduces from  $\sim 16\text{ ns}$  (perovskite/ $\text{SnO}_2$ ) to  $\sim 5\text{ ns}$  (perovskite/ $\text{SnO}_2$ /PCBM) (Figure 1d, Table S3), as compared to  $12.77\text{ ns}$  (perovskite/PCBM/ $\text{SnO}_2$ ). Combining with the TRPL data obtained for  $\text{Cu:NiO}_x$ /2-PACz/Perovskite, we confirm that a fast and balanced carrier-charge transfer (4.88 ns for  $\text{Cu:NiO}_x$ /2-PACz/Perovskite and 5.00 ns for Perovskite/ $\text{SnO}_2$ /PCBM, respectively) across these two interfaces has been established.

To understand the origins of improved charge transfer at the perovskite/ETM interfaces, we first studied the morphology of various ETMs via scanning electron microscope (SEM) and atomic force microscopy (AFM). Compared with the pristine perovskite, the  $\text{SnO}_2$ /PCBM shows the lowest root mean square (RMS) roughness value among all candidates ( $17.1 \pm 1.2\text{ nm}$ , Figure S1), indicating excellent film coverage on the perovskite layer.

We further modified the interface energetics and band alignment between the perovskite and CTMs. For the contact between perovskite and  $\text{Cu:NiO}_x$ /2-PACz, several positive impacts brought by 2-PACz have been confirmed including enhanced interfacial contact, well-aligned energy level with the perovskite, improved crystallization, etc.<sup>[31,56]</sup> However, the contact between perovskite and  $\text{SnO}_2$  has rarely been explored in IPSCs. Generally, The energy band mismatch in PSCs is a major challenge that leads to poor device performance,<sup>[57]</sup> and the exact bandgap of the resultant  $\text{SnO}_2$  is closely

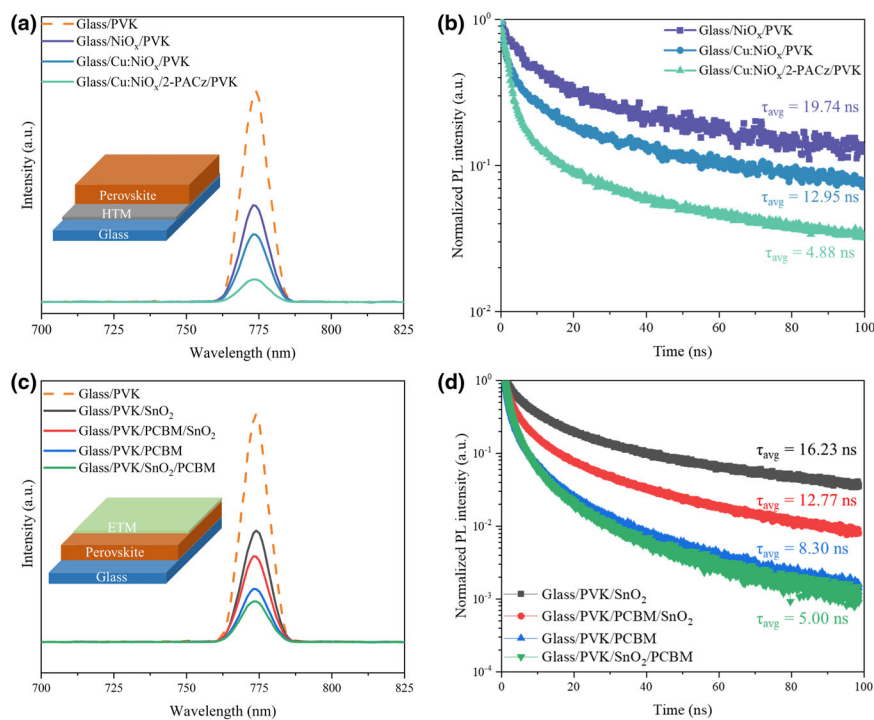


**Figure 1.** a) PL spectra of perovskite on different HTMs (Glass/perovskite, Glass/ $\text{NiO}_x$ /perovskite, Glass/ $\text{Cu:NiO}_x$ /perovskite, Glass/ $\text{Cu:NiO}_x$ /2-PACz/perovskite), the inset picture demonstrates the semi-stack HTM-based device. b) TRPL results of the perovskite with various HTMs (Glass/ $\text{NiO}_x$ /perovskite, Glass/ $\text{Cu:NiO}_x$ /Perovskite, Glass/ $\text{Cu:NiO}_x$ /2-PACz/perovskite). c) PL data of perovskite with different ETMs, (Glass/perovskite, Glass/perovskite/ $\text{SnO}_2$ , Glass/perovskite/PCBM/ $\text{SnO}_2$ , Glass/perovskite/PCBM and Glass/perovskite/ $\text{SnO}_2$ /PCBM), the inset picture presents the half-stack ETM-based device. And d) corresponding TRPL curves of perovskite with various ETMs (Glass/perovskite/ $\text{SnO}_2$ , Glass/perovskite/PCBM/ $\text{SnO}_2$ , Glass/perovskite/PCBM and Glass/perovskite/ $\text{SnO}_2$ /PCBM). (PVK = perovskite).

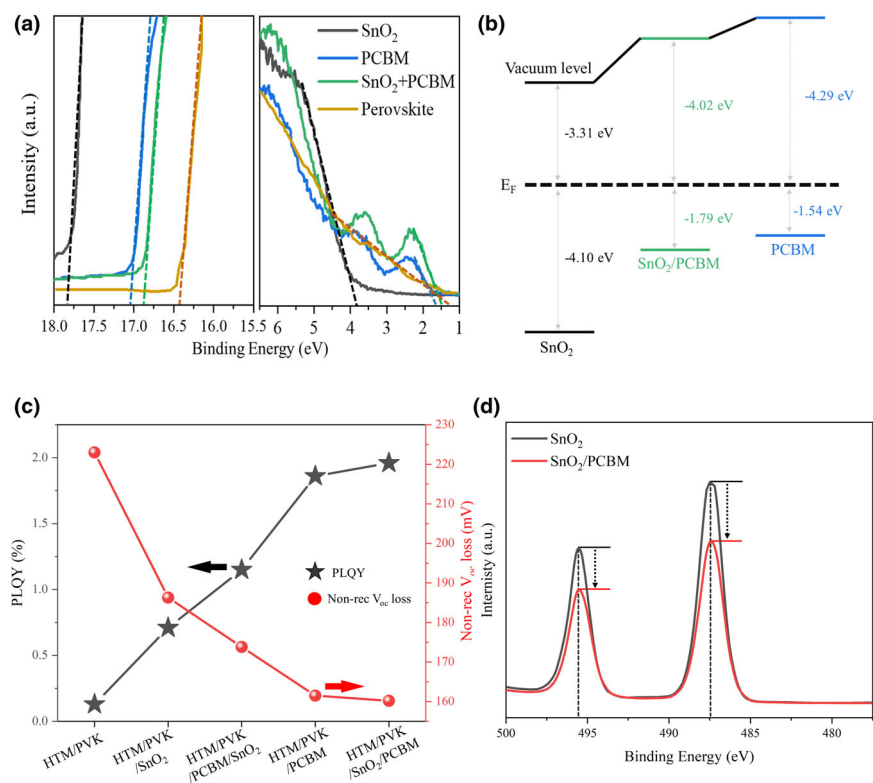
associated with the deposition routes. For instance, the conduction band (CB) and valence band (VB) of  $\text{SnO}_2$  layer prepared by ALD are  $-4.26$  and  $-7.86$  eV, respectively, while the CB and VB of the  $\text{SnO}_2$  prepared by E-beam are  $-4.06$  and  $-8.56$  eV, respectively.<sup>[58,59]</sup> To determine the band edge energies of  $\text{SnO}_2$ , PCBM and  $\text{SnO}_2$ /PCBM, ultraviolet photoelectron spectroscopy (UPS) was carried out (Figure 2a, full UPS data can be found in Figure S2), and the results of each material are illustrated in Figure 2b, where an assumed fixed Fermi level is presented.<sup>[60]</sup> Compared to the  $\text{SnO}_2$  and PCBM, the conduction band of  $\text{SnO}_2$ /PCBM presents better band alignment with the perovskite (Table S4). To further validate this speculation, photoluminescence quantum yield (PLQY) was measured. As we show in Figure 2c, the PLQY value of 1.94% for the  $\text{SnO}_2$ /PCBM-based stack is the highest among these five semi-devices. This observation is in good agreement with our speculation. Moreover, as depicted in the X-ray photoelectron spectroscopy (XPS) spectra (Figure 2d), the intensity change is predominantly related to the  $\text{SnO}_2$ -PCBM interactions. Since the binding energies of the Sn 3d do not shift too much, we speculate that the PCBM is likely to distribute between the  $\text{SnO}_2$  NPs rather than form a continuous and compact layer on top of the  $\text{SnO}_2$ . We assign this reduction of intensity to the decreased oxygen level of the  $\text{SnO}_2$ /PCBM surface. Because the PCBM is naturally hydrophobic, working as a  $\text{O}_2$  barrier, which prevents direct contact between  $\text{O}_2$  and underlying  $\text{SnO}_2$ , as a result, both Sn intensity and  $\text{O}_2$  intensity are reduced ( $\text{O}1s$  XPS can be found in

Figure S3). Another reason is that the XPS intensity also depends on the depth distribution of atoms. With a PCBM layer on top, the  $\text{SnO}_2$  layer is buried underneath, which partially contributes to the reduced intensity of the  $\text{SnO}_2$ /PCBM sample.<sup>[61]</sup>

The formation of surface dipoles is primarily responsible for the increase in the  $\text{SnO}_2$  work function after PCBM fabrication, which is known as a strong electron acceptor with a high electron affinity (3.90 eV).<sup>[62]</sup> Hence, once deposited on a low work function substrate, the PCBM layer withdraws electrons from the photoactive material and creates dipoles at the interface, contributing to the elevated work function of the  $\text{SnO}_2$  layer.<sup>[63,64]</sup> Therefore, the  $\text{SnO}_2$ /PCBM combination can harvest photogenerated electrons more efficiently from the perovskite active layer.

We then integrated  $\text{Cu:NiO}_x$ /2-PACz, a perovskite layer with a bandgap of 1.62 eV and different ETMs into IPSCs and measured the device performance characteristics. The cross-sectional SEM of a device architecture of ITO/ $\text{Cu:NiO}_x$ /2-PACz/perovskite/ETM/BCP/Ag is shown in Figure 3a, where we identify the  $\text{SnO}_2$ /PCBM forms a compact layer on top of the perovskite. For the photovoltaic performance of the devices, a champion device equipped with  $\text{Cu:NiO}_x$ /2-PACz and  $\text{SnO}_2$ /PCBM presents an outstanding PCE of 23.5% ( $V_{oc} = 1.20$  V,  $J_{sc} = 23.66$   $\text{mA cm}^{-2}$ , fill factor = 82.96%) (Figure 3b), which is

the highest PCE among all-metal-oxide-based PSCs so far (Figure S4). Additionally, thanks to the fast and balanced charge transfer at HTM/Perovskite and perovskite/ETM interfaces, the hysteresis was negligible when using  $\text{SnO}_2$ /PCBM as the ETM. The short-circuit current density ( $J_{sc}$ ) values derived from external quantum efficiency (EQE) spectra in Figure 3c are close to those obtained from current density–voltage ( $J$ - $V$ ) measurements (23.17  $\text{mA cm}^{-2}$  for  $\text{SnO}_2$ /PCBM-based devices, while 21.05  $\text{mA cm}^{-2}$  for the PCBM-only devices). The stabilized power output (SPO) also implied exceptional performance of the champion IPSCs (Figure 3d). Compared with the PCBM-only group,  $\text{SnO}_2$ /PCBM-based IPSCs stayed almost unchanged after operating for  $\sim 25$  min under one sun illumination, while the PCBM-only devices demonstrated a slight decrease in the first 4 min. Furthermore, the environmental stability of  $\text{SnO}_2$ /PCBM-based IPSCs has been enhanced significantly (Figure 3f), which could preserve over 95% of their original PCE after 1-month storage while the PCBM-only IPSCs could only retain  $\sim 60\%$  (temperature = 25 °C, relative humidity = 45%, dark, unencapsulated). The enhanced environmental stability of the  $\text{SnO}_2$ /PCBM-based IPSCs is closely related to the formation of the dense and compact  $\text{SnO}_2$ /PCBM layer on top of the perovskite layer which prevents the infiltration of oxygen and moisture, and the ion migration can be suppressed as well.<sup>[41,61]</sup> As a result, both the thermal and photostability of the resultant IPSCs have been boosted. As for the thermal stability,  $\text{SnO}_2$ /PCBM-based IPSCs reserved 80% of the pristine PCEs after 2 weeks under 85 °C, while the PCBM-only counterparts



**Figure 2.** a) Ultraviolet photoelectron spectroscopy (UPS) spectra measured with photon energy of 21.22 eV on the SnO<sub>2</sub>, PCBM, SnO<sub>2</sub>/PCBM and perovskite (underlying layers of all ETM samples are glass/ITO/Cu:NiO<sub>x</sub>/PVK), showing secondary electron cut-off and valence band region, respectively. b) Energy diagram of different ETMs, assuming a fixed Fermi level. c) Plot of the variation of photoluminescence quantum yield (PLQY) and corresponding non-recombination V<sub>oc</sub> loss of HTM/PVK, HTM/PVK/SnO<sub>2</sub>, HTM/PVK/PCBM, HTM/PVK/PCBM/SnO<sub>2</sub>, and HTM/PVK/SnO<sub>2</sub>/PCBM. d) X-ray photoelectron spectroscopy (XPS) scan spectra of the Sn 3d core level for pristine SnO<sub>2</sub> and SnO<sub>2</sub>/PCBM. (PVK = perovskite).

have turned yellowish entirely (Figure S5). Regarding photostability, SnO<sub>2</sub>/PCBM-based devices reserved the highest performance among all the devices after being exposed to 1 sun for 1000 h (SnO<sub>2</sub>/PCBM-based IPSCs maintain over 90% of their initial PCE, while the PCBM-only IPSCs can only retain ~60%) (Figure S6). In addition, the SnO<sub>2</sub>/PCBM-based IPSCs illustrated higher PCEs and smaller deviations than other groups, highlighting improved reproducibility (Figure 3e).

We summarized the champion photovoltaic performances of IPSCs based on different ETMs in Table 1. The origins of such an impressive PCE enhancement can be ascribed as follows. The primary source is associated with improved charge transfer behavior. Normally series resistance ( $R_s$ ) and shunt resistance ( $R_{sh}$ ) are used to reveal the charge transfer behaviors directly.<sup>[65]</sup> Note the devices presented are in an identical configuration except for the ETMs. Consequently, the changes of  $R_s$  and  $R_{sh}$  can be attributed to the choices of ETMs. As illustrated in Figure 4a (20 devices for each configuration), we record a reduction in  $R_s$  ~ 160  $\Omega$  to ~55  $\Omega$  upon the addition of PCBM ontop/beneath the SnO<sub>2</sub> layer. This result indicates the charges flow more efficiently in the SnO<sub>2</sub>/PCBM structure compared to that of the single ETM, which is consistent with the PL and TRPL data presented in Figure 1a–d. The relatively high  $R_s$  value recorded for SnO<sub>2</sub>-only IPSCs is consistent with metal oxide films prepared at lower temperatures which exhibit high defect densities and poor crystallinity, reducing the conductivity.<sup>[53]</sup> In

contrast to the SnO<sub>2</sub>-only IPSCs, the low  $R_s$  recorded for PCBM-only films can be attributed to the better contact between perovskite and PCBM. The roles of PCBM in IPSCs are mainly twofold: 1) suppressing the ionic migration caused by the external electric field and immobilizing the iodine ions or vacancies in the bulk of the perovskite layer, and 2) the high electron extractability of PCBM could facilitate the electron transfer at the perovskite/PCBM interface.<sup>[66]</sup> We infer that combining the PCBM which has high electron extractability but low electron mobility,<sup>[67,68]</sup> with inorganic SnO<sub>2</sub> which has high electron mobility, could help facilitate charge transfer at the perovskite/ETM interface. Interestingly, we find that the PCE of the PCBM/SnO<sub>2</sub>-based IPSCs was lower than that PCBM-only IPSCs. As the PCBM is deposited prior to the SnO<sub>2</sub> layer for PCBM/SnO<sub>2</sub>-based IPSCs, the post-annealing of SnO<sub>2</sub> layer (40 min at 100 °C) is likely to shrink the predeposited PCBM layer.<sup>[54,55]</sup> The negative impact of thermal annealing could be avoided while adopting SnO<sub>2</sub>/PCBM as the ETM where the annealing of SnO<sub>2</sub> layer is conducted prior to the deposition of PCBM. Moreover, the direct contact of fullerene and perovskite could introduce deep traps at the interface,<sup>[69,70]</sup> contributing to the higher non-radiative recombination rate and PCE drop in the PCBM/SnO<sub>2</sub>-based devices.<sup>[71]</sup> In addition, conformal coating an ultrathin (<10 nm, estimated from the XPS data, Figure 2f) PCBM layer on top of a relatively rough perovskite layer is still challenging. Therefore, we expected that SnO<sub>2</sub> NPs

could help to smooth the surface of the perovskite layer, providing a comparatively flat substrate to deposit the following layers, which is supported by the AFM analysis (Figure S1a–e). Furthermore, dark J-V curves also demonstrated the current leakage was minimized for SnO<sub>2</sub>/PCBM-based IPSCs, indicating the efficient charge transfer and mitigated current loss (Figure 4b), which is in agreement with the trend of the  $R_{sh}$  statistics.

To further explore the charge extraction occurring between the perovskite and the modified ETMs, electrochemical impedance spectra (EIS) were recorded. Among these four types of IPSCs based on different ETMs, SnO<sub>2</sub>/PCBM-based ones presented the lowest charge transfer resistance ( $R_{ct}$ ), which is 148.4  $\Omega$ , as compared to 187.2  $\Omega$  for PCBM-only, 313.0  $\Omega$  for PCBM/SnO<sub>2</sub>-based, and 513.5  $\Omega$  for SnO<sub>2</sub>-only IPSCs. (Figure 4c, the equivalent circuit can be found in Figure S7). We note that  $R_{ct}$  often includes all the factors related to charge injection and transfer processes within devices.<sup>[72]</sup> Hence, from the EIS results, we concluded that by using Cu:NiO<sub>x</sub>/2-PACz and SnO<sub>2</sub>/PCBM, a fast and balanced carrier transfer system can be created, contributing to the reduced charge transfer resistance, which is consistent with the TRPL results. We assigned the improved electrical properties of Cu:NiO<sub>x</sub>/2-PACz and SnO<sub>2</sub>/PCBM to their high charge mobility and efficient charge extraction across the interfaces. The electron mobility was determined by the space-charge limited current (SCLC) method (the



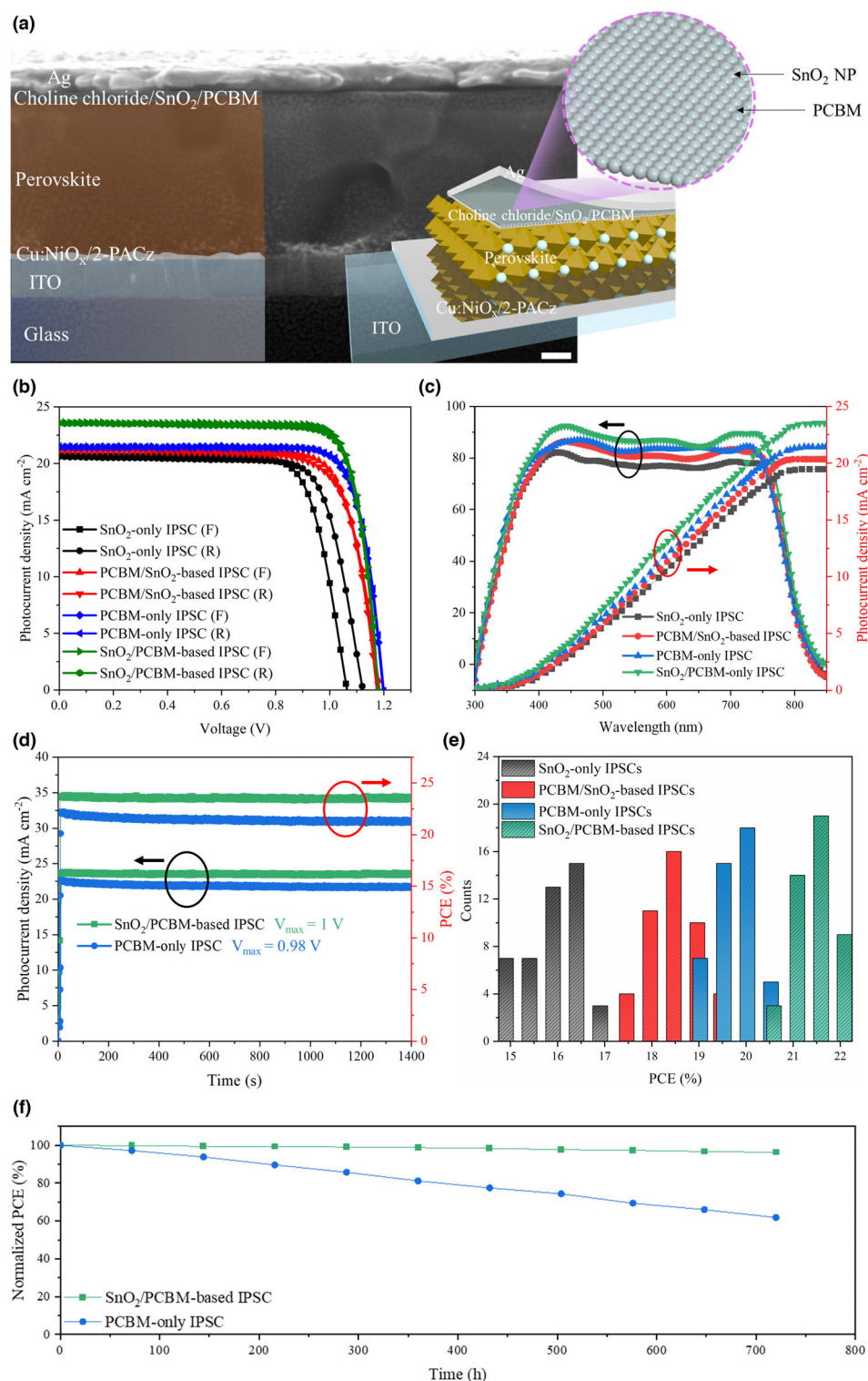


**Figure 3.** a) Cross-sectional SEM of a  $\text{SnO}_2/\text{PCBM}$ -based IPSC and illustration of the  $\text{SnO}_2/\text{PCBM}$  layer in IPSCs (scale bar = 100 nm). b)  $J$ - $V$  curves of IPSCs based on different ETMs ( $\text{SnO}_2$ -only, PCBM-only, PCBM/ $\text{SnO}_2$ , and  $\text{SnO}_2/\text{PCBM}$ , F: forward scan; R: reverse scan). c) EQE curves of  $\text{SnO}_2$ -only, PCBM/ $\text{SnO}_2$ -based, PCBM-only and  $\text{SnO}_2/\text{PCBM}$ -based IPSCs. d) SPO tracking of  $\text{SnO}_2/\text{PCBM}$ -based and PCBM-only devices. e) Reproducibility statistics of IPSCs based on various ETMs. f) Environmental stability of  $\text{SnO}_2/\text{PCBM}$ -based and PCBM-only devices. All the devices were stored in a cabinet where temperature = 25 °C, relative humidity = 45%.

structure is ITO/Ag/ETM/Ag, and the details can be found in SI).<sup>[73,74]</sup> As illustrated in Figure 4d, the  $\text{SnO}_2/\text{PCBM}$  system yielded the highest electron mobility of  $8.17 \times 10^{-2} \text{ cm}^2 \text{ V}^{-1} \text{ s}^{-1}$ , while the values of PCBM,  $\text{SnO}_2$  and PCBM/ $\text{SnO}_2$  are  $3.82 \times 10^{-3} \text{ cm}^2 \text{ V}^{-1} \text{ s}^{-1}$ ,  $2.08 \times 10^{-3} \text{ cm}^2 \text{ V}^{-1} \text{ s}^{-1}$  and  $4.37 \times 10^{-3} \text{ cm}^2 \text{ V}^{-1} \text{ s}^{-1}$ , respectively, which are in agreement with previous reports.<sup>[74–76]</sup> The dominant reason for the low charge mobility of the pristine  $\text{SnO}_2$  layer is attributed to its non-stoichiometric and trap-rich nature. After combining with PCBM, the charge mobility is enhanced, and we believe such improvement is because PCBM can help to build connective highways for carriers to move between  $\text{SnO}_2$  NPs. Except for the high electron mobility of the  $\text{SnO}_2/\text{PCBM}$ , the device performance difference between the  $\text{SnO}_2/\text{PCBM}$ -based and PCBM/ $\text{SnO}_2$ -based IPSCs is also of interest. Despite the morphology difference and fabrication sequence of PCBM and  $\text{SnO}_2$ , C=O group of the PCBM also can passivate the electron-poor oxygen vacancy defects which may help to reduce trapping and enhance the conductivity of the  $\text{SnO}_2$  layer.<sup>[77]</sup> Furthermore, we measured the light intensity dependence of the  $V_{\text{oc}}$  for champion IPSCs based on various ETMs, respectively. The light intensity dependence of  $V_{\text{oc}}$  gives insights into the primary recombination mechanism in solar cells via extracting the ideality factor ( $n$ ) from the slope  $nkT/q$  of the voltage dependence.<sup>[78,79]</sup> Thanks to the superior electron transfer of  $\text{SnO}_2/\text{PCBM}$ , the trap-assisted recombination in  $\text{SnO}_2/\text{PCBM}$ -based device ( $1.18kT/q$ ) is reduced as compared to the PCBM-only ( $1.36kT/q$ ) (Figure 4f), PCBM/ $\text{SnO}_2$ -based ( $1.42kT/q$ ) and  $\text{SnO}_2$ -only ( $1.51kT/q$ ) devices (the corresponding data are listed in Table S5), which agrees with our PLQY results (Figure 2c).

Because the fabrication temperature of the entire device is no more than 100 °C, we thus attempted to make flexible inverted perovskite

**Table 1.** Photovoltaic parameters of the champion IPSCs based on SnO<sub>2</sub>-only, PCBM-only, PCBM/SnO<sub>2</sub>, and SnO<sub>2</sub>/PCBM.

ETM	Scan direction	V <sub>oc</sub> (V)	J <sub>sc</sub> (mA cm <sup>-2</sup> )	FF (%)	PCE (%)	HI
SnO <sub>2</sub> -only	Forward	1.06	20.70	75.72	16.54	0.044
	Reverse	1.12	20.54	75.85	17.31	
PCBM/SnO <sub>2</sub>	Forward	1.17	21.11	75.81	18.72	0.035
	Reverse	1.18	21.23	77.45	19.40	
PCBM-only	Forward	1.18	21.38	80.05	20.17	0.015
	Reverse	1.18	21.51	80.69	20.48	
SnO <sub>2</sub> /PCBM	Forward	1.20	23.51	82.75	23.32	0.009
	Reverse	1.20	23.66	82.96	23.53	

J<sub>sc</sub>, short-circuit current density; V<sub>oc</sub>, open-circuit voltage; FF, fill factor; PCE, power conversion efficiency.

solar cells (f-IPSCs) based on the same device configuration. Consequently, we have achieved a champion PCE of over 21% (Figure S8, V<sub>oc</sub> = 1.17 V, J<sub>sc</sub> = 23.11 mA cm<sup>-2</sup>, FF = 79.05% and PCE = 21.37%), as compared to PCE ~19% for PCBM-only f-PSCs (Figure S9, V<sub>oc</sub> = 1.14 V, J<sub>sc</sub> = 21.36 mA cm<sup>-2</sup>, FF = 77.72% and PCE = 18.92%). Additionally, thanks to the stable SnO<sub>2</sub> NPs and the hydrophobic PCBM layer, the shelf storage stability (temperature = 25 °C, relative humidity = 45%, dark, unencapsulated) has been enhanced (Figure S10). However, we note that the shelf storage stability f-IPSCs is inferior to their rigid counterparts, which is mainly attributed to the high water vapor transmission rate (~40 °C, ~7 g m<sup>-2</sup> day<sup>-1</sup> polyethylene naphthalate, while the value is ~10<sup>-5</sup> g m<sup>-2</sup> day<sup>-1</sup> for glass) of plastic substrates.<sup>[80]</sup>

In conclusion, our research provides a feasible route to manufacture high-performance IPSCs based on metal oxides via a simple and cost-effective method. By coupling n-type SnO<sub>2</sub> with p-type Cu:NiO<sub>x</sub> as the major components of CTMs, we attained a remarkable PCE of 23.5% for IPSCs, in conjugation with the significantly enhanced long-term stability against light, heat and moisture due to the protection of metal oxides. The work highlights the importance of interfacial management in the metal oxide/perovskite interfaces, in particular when these metal oxide layers are prepared at low temperatures. We emphasize that the charge transfer balance for holes and electrons needs to be meticulously designed, to mitigate the recombination losses at the interfaces adjacent to the perovskite photoactive layer. Finally, the robust and compact metal oxide CTMs in IPSCs may offer unique advantages for flexible and tandem devices for future commercial applications.

### 3. Experimental Section

**Materials:** ITO-patterned glass substrates (10 Ω sq<sup>-1</sup>) were purchased from Huananxiangcheng Ltd. (China). Nickel (II) nitrate hexahydrate (98%) was purchased from Alfa Aesar. Sodium hydroxide (99.9%) and pH paper stick indicator were purchased from Fisher Sci Ltd. Lead diiodide (PbI<sub>2</sub>, 99.99%), [2-(9H-Carbazol-9-yl)ethyl]phosphonic Acid (2-PACz) and lead dibromide (PbBr<sub>2</sub>, 99%) were purchased from Tokyo Chemical Industry Co., Ltd. (TCI, Japan). Cesium iodide (CsI, 99.999%), Copper (II) nitrate trihydrate (98%), formamidinium iodide (FAI), methylammonium iodide (MAI), and choline chloride (≥99%) were purchased from Sigma-Aldrich. PC<sub>61</sub>BM (99.5%) and Bathocuproin (BCP, 98%) were purchased from Ossila. N,N-dimethylformamide (DMF, 99.8%), dimethyl sulfoxide (DMSO, 99.7%), chlorobenzene (CB, 99.8%) and toluene (99.85%), and

isopropanol (IPA, 99.5%) were purchased from Acros. SnO<sub>2</sub> (2.5 wt%) in butanol solution was purchased from Avantama. Filter papers were purchased from Whatman Inc. All chemicals and materials were purchased from commercial suppliers and used as received.

**Hole transport layer preparation:** 0.25 mol nickel (II) nitrate hexahydrate and copper (II) nitrate trihydrate were dissolved in 50 mL distilled water with continuous stirring, copper (II) nitrate trihydrate was added to the nickel (II) nitrate hexahydrate solution at a molar ratio of 5%. After the solution turns dark green clear, the pH value is adjusted to 10 by adding 10 M sodium hydroxide, the pH value is determined by pH indicator. The solution is kept stirring for another 15 min after pH reached 10. Then the solution is filtered by a filter paper to collect the dark green precipitation. The collected precipitation is heated at 80 °C for 1 h after washing with distilled water three times. To obtain copper-doped nickel oxide nanoparticles (Cu:NiO<sub>x</sub> NPs), the heated precipitation was transferred to a furnace to calcinate at 275 °C for 2 h to obtain black powders. Finally, the black powder was dispersed in deionized water to form 2 wt% Cu: NiO<sub>x</sub> NPs solution.

**Perovskite solar cell fabrication:** ITO-patterned glass substrates (10 Ω sq<sup>-1</sup>, Huananxiangcheng Ltd.) were cleaned with deionized water, acetone, and isopropyl alcohol, respectively. Then ITO-patterned glass substrates were treated with an oxygen plasma process (Emitech K1050X, 230 V, 100 W) for 5 min before fabrication. Cu:NiO<sub>x</sub> NPs solution was spin-coated on ITO-coated substrates at 2000 rpm (1000 rpm/s) for 20 s, followed by a post-heating process at 120 °C for 10 min. Then, these Cu:NiO<sub>x</sub>-coated substrates were moved to a UV-ozone cleaning device to receive 5 min of UV-Ozone treatment. Then the 2-PACz was prepared on top of the Cu:NiO<sub>x</sub> via spin-coating, the spin-coating condition of the 2-PACz layer is 3000 rpm (1000 rpm/s), 30 s with a solution concentration of 0.33 mg/mL (in ethanol), and baked at 100 °C for 10 min. Here, the composition of perovskite layer is Cs<sub>0.05</sub>FA<sub>0.80</sub>MA<sub>0.15</sub>Pb(I<sub>x</sub>Br<sub>1-x</sub>)<sub>3</sub>, the perovskite precursor solution was prepared by dissolving 470.23 mg PbI<sub>2</sub>, 66.06 mg PbBr<sub>2</sub>, 15.59 mg CsI, 166.64 mg formamidinium iodide, and 19.15 mg methylammonium bromide in a 1 mL solution of 4:1 V/V DMF/DMSO. Then the solution was stirred overnight at room temperature. Then perovskite layer was formed by spin-coating according to a two-step protocol, 1000 rpm for 10 s and 4000 rpm for 35 s, 80 μL CB was dropped 5 seconds before the end of the second step. Then the film was heated at 100 °C for 60 min on a hotplate. A passivation layer, choline chloride was then fabricated on top of the perovskite layer at 4000 rpm (2000 rpm/s), 30 s with a solution concentration of 1 mg/mL (in IPA), and heated at 100 °C for 30 min. SnO<sub>2</sub> layer was prepared with the SnO<sub>2</sub> butanol solution, the solution was diluted with 1-butanol till the concentration becomes half of the former value. And the SnO<sub>2</sub> thin film was spin-coated with the diluted solution at 6000 rpm (2000 rpm/s), 30 s and then was baked at 100 °C for 40 min. Phenyl-C<sub>61</sub>-butyric acid methyl ester was used as the electron transport material, PC<sub>61</sub>BM (10 mg/ml in CB) was spin-coated at 2000 rpm for 20 s, and dried at 100 °C for 5 min. Afterwards, bathocuproine solution (0.5 mg/mL in IPA) was spin-coated on top of PC<sub>61</sub>BM. Finally, a 100 nm thick Ag electrode was deposited in a thermal evaporator (<3 × 10<sup>-6</sup> Torr, Moorefield thermal evaporator) to complete the fabrication process.

**Device characterization:** XRD patterns were performed using 45 kV, 40 mA Cu Kα (λ = 0.154187 nm) radiation by PANalytical X'Pert Pro, equipped with an X-ray mirror and proportional Xe detector (GM-tube). AFM images were obtained via AIST-NT SmartSPM 1000 in a tapping mode. PL data were collected by Agilent-Cary Eclipse Fluorescence Spectrophotometer. The TRPL measurements were measured using a confocal microscope setup (PicoQuant, MicroTime 200). The sample was excited by a 510-nm pulsed diode (PDL 828, PicoQuant, pulse width ~ 100 ps) with an air objective. The signals were focused onto a Hybrid PMT detector connected to a Picoquant acquisition card for time-correlated single-photon counting (time resolution of 200 ps). The J-V characteristics and SPO tracking were performed outside the glovebox at the lab condition by using a Keysight B2901A source meter under simulated one-sun AM 1.5G illumination (100 mW cm<sup>-2</sup>) with a AAA steady solar simulator (Enlitech, SS-F5-3A). Before J-V measurements, the simulator was cautiously calibrated by using a standard monocrystalline silicon solar cell with a KG-5 filter same as previously reported, to ensure the accuracy of the J<sub>sc</sub> measured from J-V scans, a mask with an aperture area of 0.09 cm<sup>2</sup> was used during the measuring process. The sweeping conditions are reverse scan (1.20 V → -0.02 V, scan rate 40 mV s<sup>-1</sup>, and no delay time), forward scan (-0.02 V → 1.20 V, scan rate 40 mV s<sup>-1</sup>, with no delay

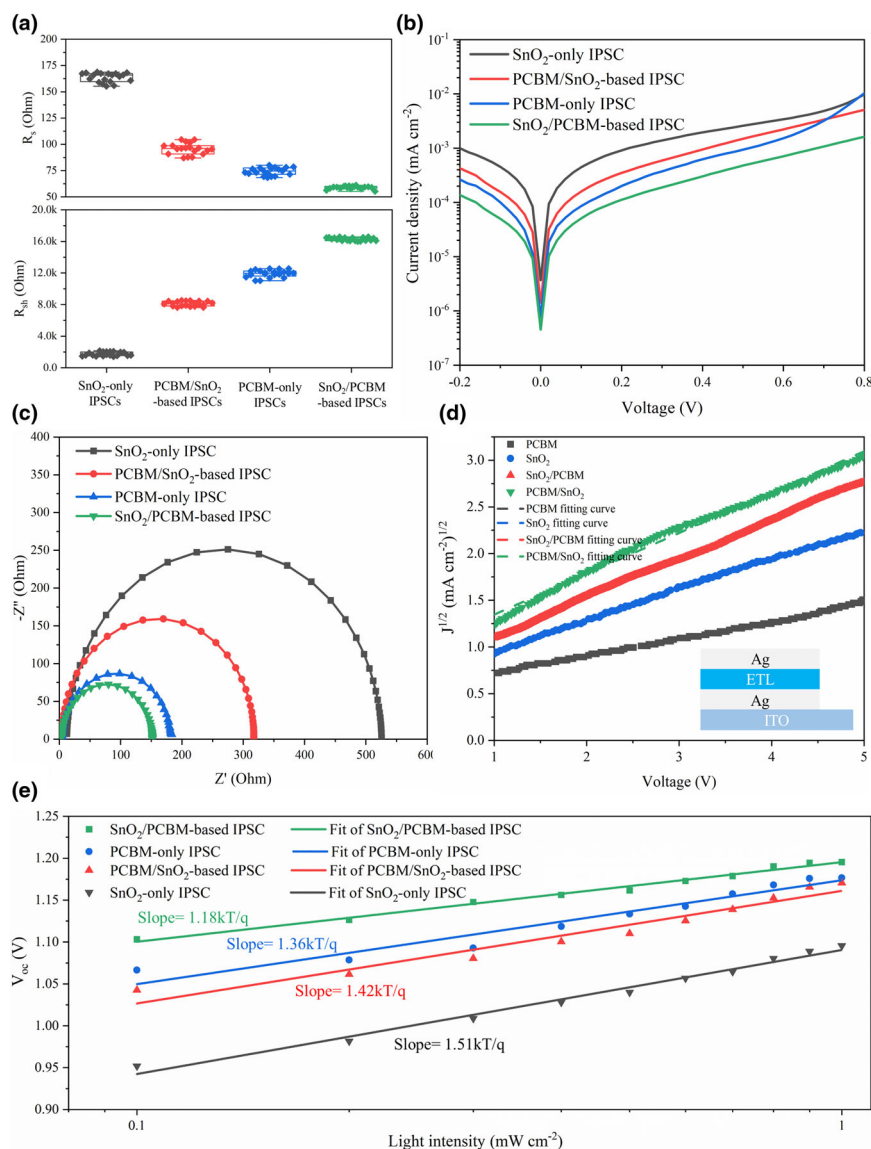


**Figure 4.** a)  $R_s$  and  $R_{sh}$  statistics of  $\text{SnO}_2$ -only, PCBM/ $\text{SnO}_2$ -only, and  $\text{SnO}_2$ /PCBM-only IPSCs. b) Dark J-V curves of IPSCs based on different ETMs. c) Nyquist plots obtained from the EIS of the  $\text{SnO}_2$ -only, PCBM/ $\text{SnO}_2$ -only, PCBM-only and  $\text{SnO}_2$ /PCBM-only IPSCs at a frequency scale of 100 k Hz to 0.1 Hz. d) SCLC measurements of  $\text{SnO}_2$ , PCBM/ $\text{SnO}_2$ , PCBM, and  $\text{SnO}_2$ /PCBM, the inset shows the device structure of ITO/Ag/ETM/Ag. e) Light intensity-dependent  $V_{oc}$  for the IPSCs with various ETMs.

time), and a reference cell purchased from Fraunhofer ISE Callab (ISE001/013–2018). All devices were measured both in the reverse scan (1.20 V  $\rightarrow$  –0.20 V, step 0.02 V, delay time 100 ms) and forward scan (–0.20  $\rightarrow$  1.20 V, step 0.02 V, delay time 100 ms) without any pre-light soaking and pre-bias process. To ensure accuracy, a mask with an aperture area of 0.09  $\text{cm}^2$  was used during the measuring process.<sup>[81,82]</sup> Data were collected by the IV testing system with software (IVS-KA5000). The light stability is measured under a 36 W LED, all the devices are stored in a  $\text{N}_2$ -filled box. For the thermal stability test, all the devices are placed on a hotplate whose temperature is set as 85  $^\circ\text{C}$  in a  $\text{N}_2$ -filled glovebox. The stabilized power output was measured at the maximum power output bias voltage. EQE was measured in air on a commercial system (Bentham PV300). And the stability test was conducted without encapsulation. The stability test was performed at 25  $^\circ\text{C}$ , and the relative humidity was  $\sim$ 45%.

## Acknowledgment

All authors discussed, analyzed, and commented on the manuscript. W.Z. acknowledges UK Engineering and Physical Sciences Research Council (EPSRC) New Investigator Award (2018; EP/R043272/1) and Newton Advanced Fellowship (192097) for financial support. K.J. and S.D.S. acknowledge funding from the Royal Society, the Engineering and Physical Sciences Research Council (EPSRC, EP/R023980/1, EP/V027131/1) and the European Research Council (ERC) under the European Union's Horizon 2020 research and innovation program (HYPERION, Grant Agreement Number 756962). S.D.S. acknowledges funding from the Royal Society and Tata Group (UF150033). J.M. and T.W. acknowledge funding from EPSRC SPECIFIC IKC (EP/N020863/1).

## Conflict of Interest

S.D.S. is a co-founder of Swift Solar Inc.

## Data Availability Statement

The data that support the findings of this study are available in the supplementary material of this article.

## Supporting Information

Supporting Information is available from the Wiley Online Library or from the author.

## Keywords

fast and balanced charge transfer, inverted perovskite solar cells, long-term stability, low-temperature processing, metal oxides

Received: December 11, 2022

Revised: January 9, 2023

Published online: January 19, 2023

[1] N.-G. Park, K. Zhu, *Nat. Rev. Mater.* **2020**, *5*, 333.

[2] Y. Deng, S. Xu, S. Chen, X. Xiao, J. Zhao, J. Huang, *Nat. Energy* **2021**, *6*, 633.

[3] Q. Jiang, J. Tong, Y. Xian, R. A. Kerner, S. P. Dunfield, C. Xiao, R. A. Scheidt, D. Kuciauskas, X. Wang, M. P. Hautzinger, R. Tirawat, M. C. Beard, D. P. Fenning, J. J. Berry, B. W. Larson, Y. Yan, K. Zhu, *Nature* **2022**, *611*, 278.

[4] H. Chen, S. Teale, B. Chen, Y. Hou, L. Grater, T. Zhu, K. Bertens, S. M. Park, H. R. Atapattu, Y. Gao, M. Wei, A. K. Johnston, Q. Zhou, K. Xu, D. Yu, C. Han, T. Cui, E. H. Jung, C. Zhou, W. Zhou, A. H. Proppe, S. Hoogland, F. Laquai, T. Filleter, K. R. Graham, Z. Ning, E. H. Sargent, *Nat. Photon.* **2022**, *16*, 352.

[5] M. Degani, Q. An, M. Albaladejo-Siguan, Y. J. Hofstetter, C. Cho, F. Paulus, G. Grancini, Y. Vaynzof, *Sci. Adv.* **2021**, *7*, eabj7930.



- [6] Z. Li, B. Li, X. Wu, S. A. Sheppard, S. Zhang, D. Gao, N. J. Long, Z. Zhu, *Science* **2022**, 376, 416.
- [7] R. Azmi, E. Ugur, A. Seitkhan, F. Aljamaan, A. S. Subbiah, J. Liu, G. T. Harrison, M. I. Nugraha, M. K. Eswaran, M. Babics, Y. Chen, F. Xu, T. G. Allen, A. U. Rehman, C. L. Wang, T. D. Anthopoulos, U. Schwingenschlogl, M. De Bastiani, E. Aydin, S. De Wolf, *Science* **2022**, 376, 73.
- [8] X. Li, W. Zhang, X. Guo, C. Lu, J. Wei, J. Fang, *Science* **2022**, 375, 434.
- [9] S. Chen, X. Dai, S. Xu, H. Jiao, L. Zhao, J. Huang, *Science* **2021**, 373, 902.
- [10] X. Luo, Z. Shen, Y. Shen, Z. Su, X. Gao, Y. Wang, Q. Han, L. Han, *Adv. Mater.* **2022**, 34, 2202100.
- [11] X. Lin, D. Cui, X. Luo, C. Zhang, Q. Han, Y. Wang, L. Han, *Energ. Environ. Sci.* **2020**, 13, 3823.
- [12] J. Príncipe, V. C. M. Duarte, L. Andrade, *Energ. Technol.* **2022**, 10, 2100952.
- [13] Q. Cao, Y. Li, H. Zhang, J. Yang, J. Han, T. Xu, S. Wang, Z. Wang, B. Gao, J. Zhao, X. Li, X. Ma, S. M. Zakeeruddin, W. E. I. Sha, X. Li, M. Grätzel, *Sci. Adv.* **2021**, 7, eabg0633.
- [14] E. H. Jung, N. J. Jeon, E. Y. Park, C. S. Moon, T. J. Shin, T.-Y. Yang, J. H. Noh, J. Seo, *Nature* **2019**, 567, 511.
- [15] D. Zhao, Z. Zhu, M.-Y. Kuo, C.-C. Chueh, A. K.-Y. Jen, *Angew. Chem. Int. Ed.* **2016**, 55, 8999.
- [16] A. F. Akbulatov, L. A. Frolova, M. P. Griffin, I. R. Gearba, A. Dolocan, D. A. Vanden Bout, S. Tsarev, E. A. Katz, A. F. Shestakov, K. J. Stevenson, P. A. Troshin, *Adv. Energy Mater.* **2017**, 7, 1700476.
- [17] J. H. Noh, S. H. Im, J. H. Heo, T. N. Mandal, S. I. Seok, *Nano Lett.* **2013**, 13, 1764.
- [18] J. H. Kim, P.-W. Liang, S. T. Williams, N. Cho, C.-C. Chueh, M. S. Glaz, D. S. Ginger, A. K.-Y. Jen, *Adv. Mater.* **2015**, 27, 695.
- [19] D. Ouyang, Z. Huang, W. C. Choy, *Adv. Funct. Mater.* **2019**, 29, 1804660.
- [20] J. You, L. Meng, T.-B. Song, T.-F. Guo, Y. Yang, W.-H. Chang, Z. Hong, H. Chen, H. Zhou, Q. Chen, Y. Liu, N. De Marco, Y. Yang, *Nat. Nanotechnol.* **2015**, 11, 75.
- [21] X. Hu, C. Liu, Z. Zhang, X. F. Jiang, J. Garcia, C. Sheehan, L. Shui, S. Priya, G. Zhou, S. Zhang, *Adv. Sci.* **2020**, 7, 2001285.
- [22] Y. Hou, X. Du, S. Scheiner, D. P. McMeekin, Z. Wang, N. Li, M. S. Killian, H. Chen, M. Richter, I. Levchuk, *Science* **2017**, 358, 1192.
- [23] M. M. Tepliakova, A. N. Mikheeva, L. A. Frolova, A. G. Boldyreva, A. Elakshar, A. V. Novikov, S. A. Tsarev, M. I. Ustinova, O. R. Yamilova, A. G. Nasibulin, S. M. Aldoshin, K. J. Stevenson, P. A. Troshin, *J. Phys. Chem. Lett.* **2020**, 11, 5563.
- [24] S. Chatterjee, A. J. Pal, *J. Phys. Chem. C* **2016**, 120, 1428.
- [25] P. Schulz, J. O. Tjepelt, J. A. Christians, I. Levine, E. Edri, E. M. Sanehira, G. Hodes, D. Cahen, A. Kahn, *ACS Appl. Mater. Interfaces* **2016**, 8, 31491.
- [26] T. Wu, L. K. Ono, R. Yoshioka, C. Ding, C. Zhang, S. Mariotti, J. Zhang, K. Mitrofanov, X. Liu, H. Segawa, R. Kabe, L. Han, Y. Qi, *Energ. Environ. Sci.* **2022**, 15, 4612.
- [27] W. Nie, H. Tsai, J. C. Blancon, F. Liu, C. C. Stoumpos, B. Traore, M. Kepenekian, O. Durand, C. Katan, S. Tretiak, *Adv. Mater.* **2018**, 30, 1703879.
- [28] S. Zhumagali, F. H. Isikgor, P. Maity, J. Yin, E. Ugur, M. De Bastiani, A. S. Subbiah, A. J. Mirabelli, R. Azmi, G. T. Harrison, J. Troughton, E. Aydin, J. Liu, T. Allen, A. U. Rehman, D. Baran, O. F. Mohammed, S. De Wolf, *Adv. Energy Mater.* **2021**, 11, 2101662.
- [29] Y.-H. Seo, I. H. Cho, S.-I. Na, *J. Alloys Compd.* **2019**, 797, 1018.
- [30] E. Aydin, J. Troughton, M. De Bastiani, E. Ugur, M. Sajjad, A. Alzahrani, M. Neophytou, U. Schwingenschlöggl, F. Laquai, D. Baran, S. De Wolf, *ACS Appl. Energy Mater.* **2018**, 1, 6227.
- [31] N. Phung, M. Verheijen, A. Todinova, K. Datta, M. Verhage, A. Al-Ashouri, H. Köbler, X. Li, A. Abate, S. Albrecht, M. Creatore, *ACS Appl. Mater. Interfaces* **2022**, 14, 2166.
- [32] K. Wang, C. Wu, Y. Hou, D. Yang, T. Ye, J. Yoon, M. Sanghadasa, S. Priya, *Energ. Environ. Sci.* **2020**, 13, 3412.
- [33] H. Min, D. Y. Lee, J. Kim, G. Kim, K. S. Lee, J. Kim, M. J. Paik, Y. K. Kim, K. S. Kim, M. G. Kim, T. J. Shin, S. Il Seok, *Nature* **2021**, 598, 444.
- [34] M. Kim, J. Jeong, H. Lu, T. K. Lee, F. T. Eickemeyer, Y. Liu, I. W. Choi, S. J. Choi, Y. Jo, H.-B. Kim, S.-I. Mo, Y.-K. Kim, H. Lee, N. G. An, S. Cho, W. R. Tress, S. M. Zakeeruddin, A. Hagfeldt, J. Y. Kim, M. Grätzel, D. S. Kim, *Science* **2022**, 375, 302.
- [35] K. Xiao, R. Lin, Q. Han, Y. Hou, Z. Qin, H. T. Nguyen, J. Wen, M. Wei, V. Yeddu, M. I. Saidaminov, Y. Gao, X. Luo, Y. Wang, H. Gao, C. Zhang, J. Xu, J. Zhu, E. H. Sargent, H. Tan, *Nat. Energy* **2020**, 5, 870.
- [36] J. J. Yoo, G. Seo, M. R. Chua, T. G. Park, Y. Lu, F. Rotermund, Y.-K. Kim, C. S. Moon, N. J. Jeon, J.-P. Correa-Baena, V. Bulović, S. S. Shin, M. G. Bawendi, J. Seo, *Nature* **2021**, 590, 587.
- [37] J. Cao, B. Wu, R. Chen, Y. Wu, Y. Hui, B.-W. Mao, N. Zheng, *Adv. Mater.* **2018**, 30, 1705596.
- [38] R. Azmi, S. Hwang, W. Yin, T.-W. Kim, T. K. Ahn, S.-Y. Jang, *ACS Energy Lett.* **2018**, 3, 1241.
- [39] G. Divitini, S. Cavovich, F. Matteocci, L. Cinà, A. Di Carlo, C. Ducati, *Nat. Energy* **2016**, 1, 1. doi: [10.1038/nenergy.2015.12](https://doi.org/10.1038/nenergy.2015.12)
- [40] P. Zhang, J. Wu, T. Zhang, Y. Wang, D. Liu, H. Chen, L. Ji, C. Liu, W. Ahmad, Z. D. Chen, S. Li, *Adv. Mater.* **2018**, 30, 1703737.
- [41] Y. Wang, C. Duan, J. Li, W. Han, M. Zhao, L. Yao, Y. Wang, C. Yan, T. Jiu, *ACS Appl. Mater. Interfaces* **2018**, 10, 20128.
- [42] Z. Zhu, Y. Bai, X. Liu, C.-C. Chueh, S. Yang, A. K.-Y. Jen, *Adv. Mater.* **2016**, 28, 6478.
- [43] A. Hultqvist, T. J. Jacobsson, S. Svanström, M. Edoff, U. B. Cappel, H. Rensmo, E. M. J. Johansson, G. Boschloo, T. Törndahl, *ACS Appl. Energy Mater.* **2021**, 4, 510.
- [44] Y. Kato, H. Fujiwara, *Hybrid Perovskite Solar Cells*, John Wiley & Sons, New York, **2021**, 563.
- [45] K. H. L. Zhang, K. Xi, M. G. Blamire, R. G. Egdell, *J. Phys. Condens. Matter* **2016**, 28, 383002.
- [46] S. Lany, J. Osorio-Guillén, A. Zunger, *Phys. Rev. B* **2007**, 75, 241203.
- [47] J. Zhang, X. Hu, H. Li, K. Ji, B. Li, X. Liu, Y. Xiang, P. Hou, C. Liu, Z. Wu, Y. Shen, S. D. Stranks, S. R. P. Silva, H.-M. Cheng, W. Zhang, *Adv. Funct. Mater.* **2021**, 31, 2104396.
- [48] Q. He, K. Yao, X. Wang, X. Xia, S. Leng, F. Li, *ACS Appl. Mater. Interfaces* **2017**, 9, 41887.
- [49] K. Yao, F. Li, Q. He, X. Wang, Y. Jiang, H. Huang, A. K. Y. Jen, *Nano Energy* **2017**, 40, 155.
- [50] J. W. Jung, C.-C. Chueh, A. K.-Y. Jen, *Adv. Mater.* **2015**, 27, 7874.
- [51] A. Al-Ashouri, A. Magomedov, M. Roß, M. Jošt, M. Talaikis, G. Chistia-kova, T. Bertram, J. A. Márquez, E. Köhnen, E. Kasparavičius, S. Lev-cenco, L. Gil-Escrig, C. J. Hages, R. Schlattmann, B. Rech, T. Malinauskas, T. Unold, C. A. Kaufmann, L. Korte, G. Niaura, V. Getautis, S. Albrecht, *Energ. Environ. Sci.* **2019**, 12, 3356.
- [52] L. Li, Y. Wang, X. Wang, R. Lin, X. Luo, Z. Liu, K. Zhou, S. Xiong, Q. Bao, G. Chen, Y. Tian, Y. Deng, K. Xiao, J. Wu, M. I. Saidaminov, H. Lin, C.-Q. Ma, Z. Zhao, Y. Wu, L. Zhang, H. Tan, *Nat. Energy* **2022**, 7, 708.
- [53] C. Altinkaya, E. Aydin, E. Ugur, F. H. Isikgor, A. S. Subbiah, M. De Bastiani, J. Liu, A. Babayigit, T. G. Allen, F. Laquai, A. Yildiz, S. De Wolf, *Adv. Mater.* **2021**, 33, 2005504.
- [54] S. M. Mortuza, S. Banerjee, *J. Chem. Phys.* **2012**, 137, 244308.
- [55] J. Xiong, N. Liu, X. Hu, Y. Qi, W. Liu, J. Dai, Y. Zhang, Z. Dai, X. Zhang, Y. Huang, Z. Zhang, Q. Dai, J. Zhang, *Adv. Energy Mater.* **2022**, 12, 2201787.
- [56] A. R. M. Alghamdi, M. Yanagida, Y. Shirai, G. G. Andersson, K. Miyano, *ACS Omega* **2022**, 7, 12147.
- [57] X. Liu, Y. Wang, F. Xie, X. Yang, L. Han, *ACS Energy Lett.* **2018**, 3, 1116.
- [58] J. P. Correa Baena, L. Steier, W. Tress, M. Saliba, S. Neutzner, T. Matsui, F. Giordano, T. J. Jacobsson, A. R. Srimath Kandada, S. M. Zakeeruddin, A. Petrozza, A. Abate, M. K. Nazeeruddin, M. Grätzel, A. Hagfeldt, *Energ. Environ. Sci.* **2015**, 8, 2928.
- [59] Z. Song, W. Bi, X. Zhuang, Y. Wu, B. Zhang, X. Chen, C. Chen, Q. Dai, H. Song, *Solar RRL* **2020**, 4, 1900266.
- [60] S. Zhang, M. Stolterfoht, A. Armin, Q. Lin, F. Zu, J. Sobus, H. Jin, N. Koch, P. Meredith, P. L. Burn, D. Neher, *ACS Appl. Mater. Interfaces* **2018**, 10, 21681.



- [61] W. Ke, D. Zhao, C. Xiao, C. Wang, A. J. Cimaroli, C. R. Grice, M. Yang, Z. Li, C.-S. Jiang, M. Al-Jassim, K. Zhu, M. G. Kanatzidis, G. Fang, Y. Yan, *J. Mater. Chem. A* **2016**, *4*, 14276.
- [62] K. Kanai, K. Akaike, K. Koyasu, K. Sakai, T. Nishi, Y. Kamizuru, T. Nishi, Y. Ouchi, K. Seki, *Appl. Phys. A* **2009**, *95*, 309.
- [63] L. Zuo, Q. Chen, N. De Marco, Y.-T. Hsieh, H. Chen, P. Sun, S.-Y. Chang, H. Zhao, S. Dong, Y. Yang, *Nano Lett.* **2017**, *17*, 269.
- [64] Y. Vaynzof, D. Kabra, L. Zhao, P. K. H. Ho, A. T.-S. Wee, R. H. Friend, *Appl. Phys. Lett.* **2010**, *97*, 033309.
- [65] D. Glowienka, Y. Galagan, *Adv. Mater.* **2022**, *34*, 2105920.
- [66] Y. Zhong, M. Hufnagel, M. Thelakkat, C. Li, S. Huettnner, *Adv. Funct. Mater.* **2020**, *30*, 1908920.
- [67] Z. Zhu, Q. Xue, H. He, K. Jiang, Z. Hu, Y. Bai, T. Zhang, S. Xiao, K. Gundogdu, B. R. Gautam, H. Ade, F. Huang, K. S. Wong, H.-L. Yip, S. Yang, H. Yan, *Adv. Sci.* **2016**, *3*, 1500353.
- [68] X. Meng, C. H. Y. Ho, S. Xiao, Y. Bai, T. Zhang, C. Hu, H. Lin, Y. Yang, S. K. So, S. Yang, *Nano Energy* **2018**, *52*, 300.
- [69] J. Warby, F. Zu, S. Zeiske, E. Gutierrez-Partida, L. Frohloff, S. Kahmann, K. Frohna, E. Mosconi, E. Radicchi, F. Lang, S. Shah, F. Peña-Camargo, H. Hempel, T. Unold, N. Koch, A. Armin, F. De Angelis, S. D. Stranks, D. Neher, M. Stolterfoht, *Adv. Energy Mater.* **2022**, *12*, 2103567.
- [70] T. Leijtens, G. E. Eperon, A. J. Barker, G. Grancini, W. Zhang, J. M. Ball, A. R. S. Kandada, H. J. Snaith, A. Petrozza, *Energ. Environ. Sci.* **2016**, *9*, 3472.
- [71] B. Roose, Q. Wang, A. Abate, *Adv. Energy Mater.* **2019**, *9*, 1803140.
- [72] F. Ebadi, N. Taghavinia, R. Mohammadpour, A. Hagfeldt, W. Tress, *Nat. Commun.* **2019**, *10*, 1574.
- [73] H. Yu, H.-I. Yeom, J. W. Lee, K. Lee, D. Hwang, J. Yun, J. Ryu, J. Lee, S. Bae, S. K. Kim, J. Jang, *Adv. Mater.* **2018**, *30*, 1704825.
- [74] Y. Luan, X. Yi, P. Mao, Y. Wei, J. Zhuang, N. Chen, T. Lin, C. Li, J. Wang, *iScience* **2019**, *16*, 433.
- [75] A. Armin, S. Shoaee, Q. Lin, P. L. Burn, P. Meredith, *npj Flex. Electron.* **2017**, *1*, 13.
- [76] S. M. Tuladhar, D. Poplavskyy, S. A. Choulis, J. R. Durrant, D. D. C. Bradley, J. Nelson, *Adv. Funct. Mater.* **2005**, *15*, 1171.
- [77] M. Yavari, X. Liu, T. Webb, K. D. G. I. Jayawardena, Y. Xiang, S. Kern, S. Hinder, T. J. Macdonald, S. R. P. Silva, S. J. Sweeney, W. Zhang, *J. Mater. Chem. C* **2021**, *9*, 4367.
- [78] Q. Jiang, Y. Zhao, X. Zhang, X. Yang, Y. Chen, Z. Chu, Q. Ye, X. Li, Z. Yin, J. You, *Nat. Photon.* **2019**, *13*, 460.
- [79] M. M. Mandoc, F. B. Kooistra, J. C. Hummelen, B. D. Boer, P. W. M. Blom, *Appl. Phys. Lett.* **2007**, *91*, 263505.
- [80] K. Ghaffarzadeh, Barrier Films and Thin Film Encapsulation for Flexible and/or Organic Electronics 2019-2029 Multi-layer barrier films, thin film encapsulation, ALD, flexible glass and beyond, **2019**, <https://www.idtechex.com/en/research-report/barrier-films-and-thin-film-encapsulation-for-flexible-and-or-organic-electronics-2019-2029/653>.
- [81] B. Li, Y. Xiang, K. D. G. I. Jayawardena, D. Luo, Z. Wang, X. Yang, J. F. Watts, S. Hinder, M. T. Sajjad, T. Webb, H. Luo, I. Marko, H. Li, S. A. J. Thomson, R. Zhu, G. Shao, S. J. Sweeney, S. R. P. Silva, W. Zhang, *Nano Energy* **2020**, *78*, 105249.
- [82] X. Yang, D. Luo, Y. Xiang, L. Zhao, M. Anaya, Y. Shen, J. Wu, W. Yang, Y.-H. Chiang, Y. Tu, R. Su, Q. Hu, H. Yu, G. Shao, W. Huang, T. P. Russell, Q. Gong, S. D. Stranks, W. Zhang, R. Zhu, *Adv. Mater.*, **2021**, *33*, 2006435.